



Land surface air temperature variations over Eurasia and possible causes in the past century

Zhiyan Zuo,^{a,b,*}  Song Yang,^{c,g}  Kang Xu,^d Renhe Zhang,^e Qiong He,^b Tianbao Zhao^f and Jing Cong^f

^a State Key Laboratory of Severe Weather, Chinese Academy of Meteorological Sciences, Beijing, China

^b Collaborative Innovation Center on Forecast and Evaluation of Meteorological Disasters, Nanjing University of Information Science and Technology, China

^c Department of Atmospheric Sciences, Sun Yat-sen University, Guangzhou, China

^d State Key Laboratory of Tropical Oceanography, South China Sea Institute of Oceanology, Chinese Academy of Sciences, Guangzhou, China

^e Institute of Atmospheric Sciences, Fudan University, Shanghai, China

^f Key Laboratory of Regional Climate-Environment Research for East Asia, Institute of Atmospheric Physics, Chinese Academy of Sciences, Beijing, China

^g School of Atmospheric Sciences and Guangdong Province Key Laboratory for Climate Change and Natural Disaster Studies, Sun Yat-sen University, Guangzhou, China

ABSTRACT: In this study, the variations of annual land surface air temperature (SAT) over Eurasia and the northern part of Africa (0°–180°E, 0°–90°N) were investigated using monthly SAT data from the Climatic Research Unit, University of East Anglia for 1901–2014 and the simulations from the Geophysical Fluid Dynamics Laboratory coupled model. The observed results suggested that the SAT variations exhibited robust non-uniform spatial features at multi-time scales. For the variations in inter-annual to decadal time scales (IDV), the intensity generally increased from south to north, with the strongest intensity being around Siberia and four times that of the weakest intensity found around China. The IDV leading pattern showed a north–south dipole across 40°N. The simulated results suggested that the north–south dipole and the northwards increase of the IDV were due to internal interactions within the complex nonlinear climate system, but the natural and greenhouse gas forcings could intensify the IDV.

The warming trend of the SAT was generally homogeneous, but it showed distinctive multi-decadal fluctuations in different regions. The linear secular trends and robust multi-decadal variation around Siberia and China corresponded to the considerable acceleration and deceleration in the warming over the two regions, respectively. The warming around Siberia was mainly caused by greenhouse gases but its modulation due to natural forcing was also considerable because of the robust multi-decadal variations. Around China, the multi-decadal variation, contributed by the natural forcing, can explain more than half the variances in the warming. The warming trend around central Asia was intense and parabolic, and the multi-decadal variation over there was weak and showed few modulating effects.

KEY WORDS land surface air temperature; warming; Eurasia; inter-annual to decadal variations; multi-decadal variation

Received 5 January 2017; Revised 25 August 2017; Accepted 1 September 2017

1. Introduction

In the past two decades, the investigations of global surface air temperature (SAT) have been a focal point because of global warming and the significant effect of the warming on oceanic and atmospheric circulation variations (e.g. Vecchi *et al.*, 2006; IPCC, 2007, 2013; Wentz *et al.*, 2007; Toggweiler and Russell, 2008; Qian *et al.*, 2010; Zuo *et al.*, 2012b). The non-monotonic features of surface air warming trends have been revealed in several recent studies. For example, Levitus *et al.* (2000) reported that the global oceans have undergone a net warming although the warming was not monotonic for 1948–2008. Ji *et al.*

(2014) suggested that a noticeable warming (>0.2 K since 1900) first took place in the subtropical and subpolar regions of the Northern Hemisphere and that the two zonal bands of warming expanded from 1950 to 1985 before merging to cover the entire Northern Hemisphere. Pepin *et al.* (2015) documented that high-mountain environments experience more rapid changes in temperature than the environments at lower elevations.

Research investigating the plausible causes for global warming has become a ‘hot spot’. Kravtsov and Spanna (2008) reported that the Atlantic multi-decadal oscillation influenced the secular trend in the global-mean surface temperature via the direct regional contribution to surface temperature evolution and via the indirect warming linked to the variability of oceanic uptake of CO₂ associated with the oceanic thermohaline circulation. Wu *et al.* (2011) showed that the rapidity of the

* Correspondence to: Z. Zuo, State Key Laboratory of Severe Weather, Chinese Academy of Meteorological Sciences, No. 46, Zhongguancun South Street, Beijing 10081, China. E-mail: zuozy@cma.gov.cn

warming in the late 20th century was the result of the concurrence of a secular warming trend and the warming phase of the multi-decadal oscillatory variation; they estimated up to one-third of the late 20th-century warming could have been the consequence of natural variability. Meehl *et al.* (2011) suggested that the deep-ocean uptake of heat could have caused the hiatus periods of the observed global-mean surface temperature. Xiao *et al.* (2012) documented that the nonlinear responses to all climate forcing (both anthropogenic and natural forcing) contributed to approximately half of the warming at the end of the 20th century over China. Booth *et al.* (2012) suggested that volcanic activity and aerosol processes can drive the pronounced multi-decadal variance in the detrended 1860–2005 North Atlantic sea surface temperature. Gao *et al.* (2015) reported that the Atlantic multi-decadal oscillation and Pacific decadal oscillation dominated the multi-decadal variability of the global land surface air temperature.

Relative to the number of studies on the SAT warming, few have paid attention to the inter-annual to decadal variations (IDV) on a hemispherical scale. Shen and Kimoto (2007) reported that the year-to-year variation in the springtime Eurasian SAT exhibited a north–south seesaw spatial pattern on the continental scale. Kang (1996) demonstrated that both the inter-annual and inter-decadal variations in the global mean temperature anomalies were associated with the corresponding variations of tropical Pacific sea surface temperature. Räisänen (2002) suggested that the gradual doubling of CO₂ led to a decrease in the temperature variability during the winter half of the year in the extra-tropical Northern Hemisphere and over the high-latitude Southern Ocean. Over land in the low latitudes and in the northern mid-latitudes in the summer, a slight tendency towards increased temperature variability occurred. Other studies focused on the IDV of the SAT over some particular regions and its effects on regional climate variability (e.g. Kang, 1996).

It is well known that the variations of SAT over Eurasian landmass are inextricably tied with the climate in the Northern Hemisphere. For example, Zuo *et al.* (2012b, 2013) documented the importance of the spatially uneven warming over the Eurasian landmass to the Asian summer monsoon. The intensive IDV of Eurasian SAT might also contribute considerably to the high-impact extreme climate events in Europe and Asia (Zuo *et al.*, 2011). Zuo *et al.* (2012a) reported that the anomalies of Eurasian SAT caused by snow cover played an important role in the rainfall over southern China in the spring. However, although the investigation of global SAT variation has become a topic of interest, most studies focused on the warming feature itself. The detailed features of Eurasian SAT variations at multi-time scales have not been carefully documented. Specifically, what were the detailed features of the Eurasian SAT IDV, multi-decadal variations and secular trend? For example, what about the leading patterns of Eurasian SAT at multi-time scales? Were there some key regions where the SAT exhibits more or less intensive variations at multi-time scales? What about the

contributions of the IDV, multi-decadal variations and secular trend to the variations in these key areas? Moreover, what are the plausible causes for these variations at multi-time scales? Motivated by these questions, the ultimate goal of this study is to understand the Eurasian SAT variations at multi-time scales and their plausible causes of these variations in the past century.

The observed data sets, model outputs and methods used in this study are described in Section 2. The observed spatial uneven features of Eurasian SAT at multi-time scales and their plausible causes are presented in Sections 3 and 4, respectively. The summary and conclusions are provided in Section 5.

2. Data, model outputs and methods

The updated gridded land-based Climatic Research Unit temperature database (CRUTEM4) for 1901–2014 is used for the observational investigation (Jones *et al.*, 2012). The CRUTEM4 comprises 5583 station records, which replaced the stations in CRUTEM3 with improved data from the National Meteorological Services. For the Northern Hemisphere, the CRUTEM4 agrees well with the ERA-40 (1958–2001) and excellently with ERA-Interim (1979–2009). Additionally, the correlations between CRUTEM4 and the temperature time series developed by the National Climatic Data Center and the temperature data set developed by the Goddard Institute for Space Studies are 0.984 and 0.980, respectively (Smith *et al.*, 2008; Hansen *et al.*, 2010).

The four data sets of the simulated SAT from the Geophysical Fluid Dynamics Laboratory (GFDL) coupled model are used to investigate the causes for the SAT variations at multi-time scales. The four data sets were, respectively, derived from the pre-industrial control run experiment (CTRL; 500 year after spin-up period), the historical experiment with all forcing (HIS), experiment with natural forcing only (NAT) and experiment with anthropogenic greenhouse gas forcing only (GHG) for 1851–2005. The CTRL is two-member ensembles and the other three sets of data sets are the four-member ensembles, with one member for the CTRL and two member for the other three experiments derived from GFDL's coupled physical model (Donner *et al.*, 2012; <https://www.gfdl.noaa.gov/coupled-physical-model-cm3/>), and one member for the CTRL and two members for the other three sets of data sets derived from the NOAA's earth system model with GFDL's modular ocean model version 4.1 (Dunne *et al.*, 2012, 2013; <https://www.gfdl.noaa.gov/earth-system-model/>).

The CTRL imposed non-evolving, pre-industrial conditions. The HIS imposed changing conditions (consistent with observations) which include atmospheric composition (including CO₂) due to both anthropogenic and volcanic influences, solar forcing, emissions or concentrations of natural and anthropogenic aerosols and their precursors, numerous types of emissions due to natural vegetation change and land use. For NAT, the imposed conditions

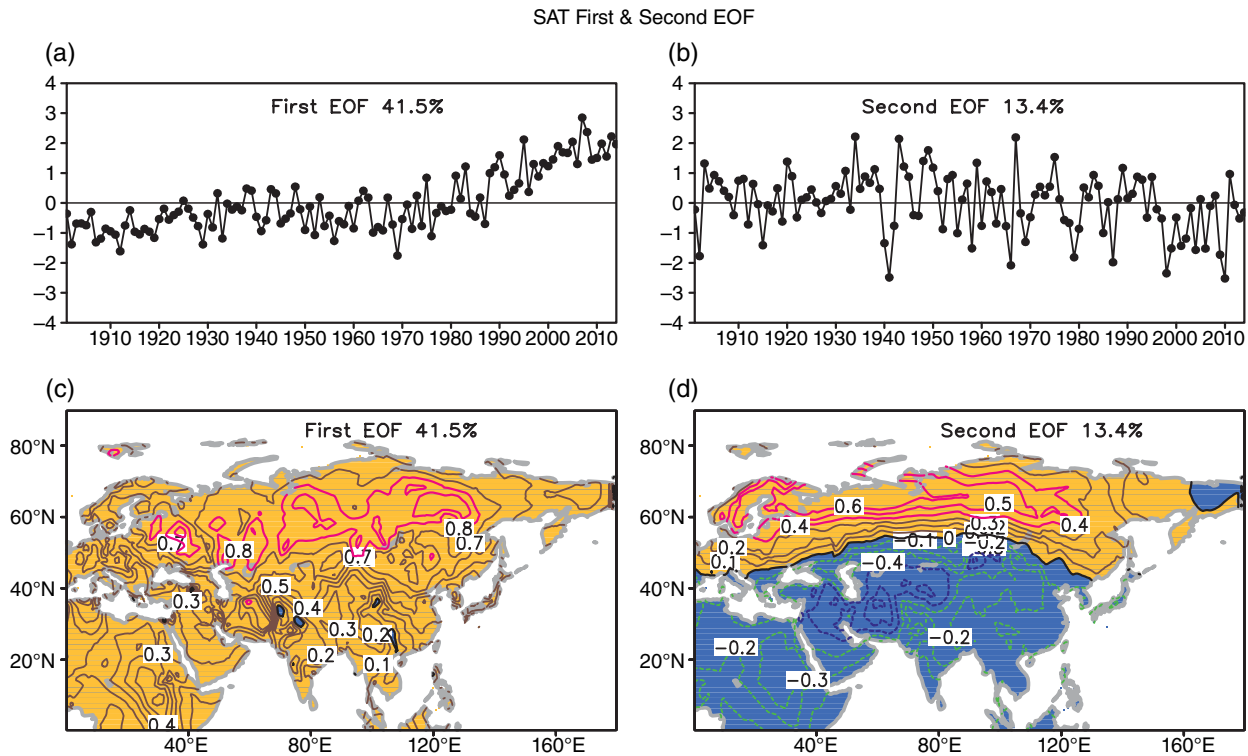


Figure 1. Spatial distribution (bottom) and the associated principal components (top) of the first EOF (left) and second EOF (right) modes of the SAT over Eurasia and the northern part of Africa. [Colour figure can be viewed at wileyonlinelibrary.com].

are the same as in the CTRL, but with natural forcing (e.g. volcanoes and solar variability) evolving as the HIS. The GHG imposed the same conditions as in the CTRL, but with the greenhouse gas forcing evolving as in the HIS. This can yield an estimate of the contribution of greenhouse gas forcing on recent warming (http://cmip-pcmdi.llnl.gov/cmip5/docs/Taylor_CMIP5_design.pdf).

Empirical orthogonal function (EOF) analysis is used to examine the spatial and temporal characteristics of SAT over Eurasia and the northern part of Africa. The ensemble empirical mode decomposition (EEMD) method is a self-adaptive analysis method that decomposes a time series into several oscillatory components on various time scales and a nonlinear secular trend, which is used to extract signals of SAT variations at various times scales in this study. Specifically, an ensemble size of 1000 and a white noise with an amplitude of 0.2 times the standard deviation of the annual SAT series are used to conduct the EEMD (Wu *et al.*, 2011). The observed SAT time series (1901–2009) is decomposed into five intrinsic mode functions (IMFs) and a residual secular trend, and the modelled SAT time series (1861–2005) is decomposed into six IMFs and a residual secular trend.

3. Observed variability

Figure 1 shows the spatial distribution and the corresponding time series of the first EOF mode and the second EOF mode of the SAT over Eurasia and the northern part of Africa (0°–180°E, 0°–90°N). The leading two patterns

can explain more than 50% of the total variance (41.5% for the first EOF mode and 13.4% for the second EOF mode). The prominent feature in the leading EOF mode was the homogeneous warming trend over most parts of Eurasia and northern Africa (Figure 1(b)). Nevertheless, the uneven features of the warming trend were also distinct. The maximum warming was located across the zonal belt of 50°–70°N and was larger than 0.8 K, whereas the minimum warming south of 40°N in China was less than 0.3 K. In terms of its temporal evolution, the warming was obviously accelerated after the 1980s (Figure 1(a)). The spatial distribution of the second EOF mode had a north–south dipole structure across ~50°N. The SAT north of 50°N was anomalously warm while the SAT south of 50°N was anomalously cold. The maximum negative anomalies were located over central Asia (CA) and the maximum positive anomalies were located over northern Europe and Siberia (Figure 1(d)). The corresponding time series showed intensive inter-annual fluctuations and robust variability on a decadal time scale (Figure 1(c)). Generally, the inter-annual fluctuation was relatively moderate before 1940 and became intense afterwards.

To further analyse the variations of SAT in the two leading EOF modes, we decomposed their associated time series using EEMD. Figure 2 shows the time series of each IMF and the secular trends of the first and second EOFs, and Table 1 exhibits the variance explained by each IMF and the secular trend. As expected, the secular trend explained the maximum variance of the first EOF (67.8%), indicating that the homogenous but spatially uneven variation of SAT was mainly contributed to

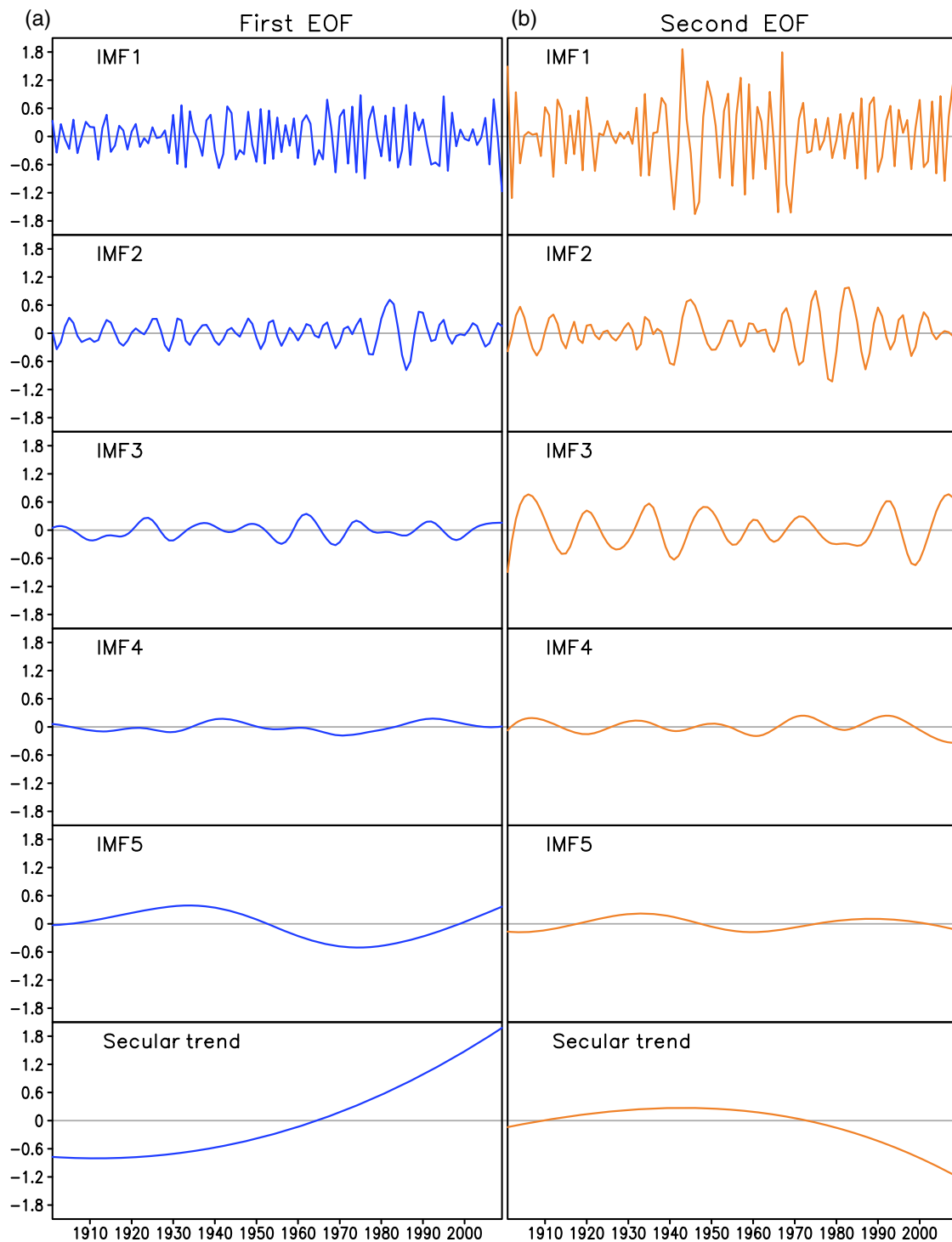


Figure 2. EEMD decompositions of the time series of the first EOF (left) and second EOF (right). [Colour figure can be viewed at wileyonlinelibrary.com].

by the warming tendency. The inter-annual component (IMF1) explains 16.8% variance, which was the second largest amount. The 24% variance was explained by the total inter-annual to decadal components (IMF1, IMF2 and IMF3), and less than 10% of the variance was explained by the multi-decadal variation component (IMF4 and IMF5). In comparison with the variance of the first EOF, the maximum variance of the second EOF (62.5%) was explained by its inter-annual component (IMF1). Generally, IMF1

showed more intensive fluctuation in the 1940s–1970s than those before the 1940s and after the 1970s; namely, the inter-annual variations were stronger in cold periods than in warm periods. The inter-annual to decadal components explained nearly 90% of the variance of the second EOF, suggesting that the north–south dipole feature was mainly evident for inter-annual to decadal time scales.

In short, the SAT variations exhibited robust non-uniform features from the inter-annual, decadal, inter-

Table 1. EEMD decompositions of the time series of first EOF and second EOF of the SAT over Eurasia and the northern part of Africa, the SIB SAT, CHN SAT and CA SAT.

	IMF1 (%)	IMF2 (%)	IMF3 (%)	IMF4 (%)	IMF5 (%)	Secular trend (%)
First EOF	16.8	5.4	1.8	1.3	6.9	67.8
Second EOF	62.5	14.7	12.5	6.2	1.6	2.6
SIB	50.6	7.4	2.3	1.8	9.5	28.5
CHN	21.6	8.3	5.2	29.8	4.2	30.9
CA	32.4	7.2	7.4	4.5	2.8	45.6

decadal, multi-decadal time scales to the secular trend. The maximum positive anomalies were located around Siberia (SIB; 55°–70°N, 60°–120°E) in both the first and second EOF modes, while the maximum negative anomalies were located in CA (30°–45°N, 40°–80°E), and moderately negative anomalies occurred south of 40°N around China (CHN; 20°–40°N, 80°–120°E) in the second EOF mode. Wu *et al.* (2011) and Gao *et al.* (2015) also suggested that the SAT variations over the three areas exhibited distinguishable characteristics at the long-term scales, with strong secular trends but weak multi-decadal variations over SIB and CA whereas robust multi-decadal variations but moderate secular trends occurred over CHN. Thus, we were especially interested in the detailed characteristics of the SAT over the three key regions, in addition to the features of the SAT over Eurasia and the northern part of Africa at multi-time scales.

3.1. Inter-annual to decadal variations

We removed the 11-year smoothing from the original SAT to investigate the SAT IDV. The leading EOF mode of SAT IDV was illustrated in Figure 3(a), which explained 31.1% variance. As expected, the north–south dipole was the leading pattern. The negative anomalies south of 40°N were much weaker than the positive anomalies north of 40°N, indicating SAT over northern Eurasia exhibited much more intensive IDV than the SAT over southern Eurasia and the northern part of Africa. The maximum anomalies, those larger than 0.7 K, were located in the zonal belt between 50° and 70°N; namely, the SAT over northern Eurasia not only showed a more rapid warming trend but also more intensive IDV compared to the SAT over southern Eurasia and the northern part of Africa.

Considering that the cycle of IMF1 was approximately 2 years and that IMF1 explained more than 60% of the variance of the north–south dipole pattern in the second EOF mode, we further analysed the leading EOF mode of the year-to-year (Y2Y) variation of the SAT. The 32.3% variance explained by the leading EOF mode of the SAT Y2Y was slightly larger than that of SAT IDV. Generally, the spatial distribution of the SAT Y2Y in the leading EOF mode was similar to that of the SAT IDV, aside from the larger values north of 40°N (Figure 3(b)). The maximum anomalies over central Siberia were greater than 1.2 K, which is about twice of the SAT IDV variation.

Figure 4(a) shows the time series of the SAT IDV over SIB, CHN and CA. The positive SAT IDV anomalies over

SIB were associated with the negative SAT IDV anomalies over CHN, with the correlation coefficient exceeding the 95% confidence level ($R = -0.29$). The SAT IDV in CA showed significant positive relationships with that in CHN ($R = 0.42$), which was consistent with the anomalous feature in the second EOF mode (Figure 1(d)). Generally, the relation of SAT Y2Y among the three regions was similar to those of the SAT IDV, including both the significant out-of-phase relationship between those of SIB and CHN and the significant in-phase relationship between those of CHN and CA (Figure 4(b)). Overall, the north–south dipole was represented by the opposite anomalies over CHN and SIB on inter-annual to decadal time scales. The opposing features between the SAT around CA and the SAT around Siberia, as displayed in Figure 1(b), cannot be found on the inter-annual to decadal time scales. The SAT IDV over CA showed an insignificant negative relationships with SAT IDV over SIB. The spatial distributions of the second EOF mode of the SAT IDV also did not show out-of-phase relationships over CA and SIB (not shown).

Another distinguishable feature in Figure 4(a) is the fluctuation of the SAT IDV over SIB, which was much more intense than those of SAT IDV over CHN and CA. The difference between the SIB and CHN SAT Y2Y was more evident (Figure 4(b)). Specifically, the standard deviation of SAT Y2Y over SIB was nearly five times that over CHN. The standard deviation of the SAT Y2Y over CA was approximately half of that over SIB and twice that over CHN. The maximum SAT Y2Y standard deviation was located around Siberia, with a value greater than 1.4 K. The standard deviation gradually decreased southwards, with a minimum value of less than 0.4 K occurring around southern China (Figure 5(a)).

The SAT IDV did not show any intensive fluctuations in the time evolution over CHN. However, it exhibited abrupt increases in 1930, with a deviation that was generally less than 1.0 before 1930 and larger than 1.0 afterwards over SIB. Over CA, the SAT Y2Y exhibited a slightly larger deviation for 1950–1975 than those in the other periods (Figures 4(a) and (b)). The 11-year-running standard deviation of the SAT Y2Y over CA showed a robust increasing trend for 1940–1975 and decreasing trends before 1940 and after 1975 (Figure 5(b)), which was generally consistent with the IMF1 of the second EOF, as shown in Figure 2(b). The 11-year-running standard deviation of the SAT Y2Y over SIB showed similar variation to that over CA, but with a more robust

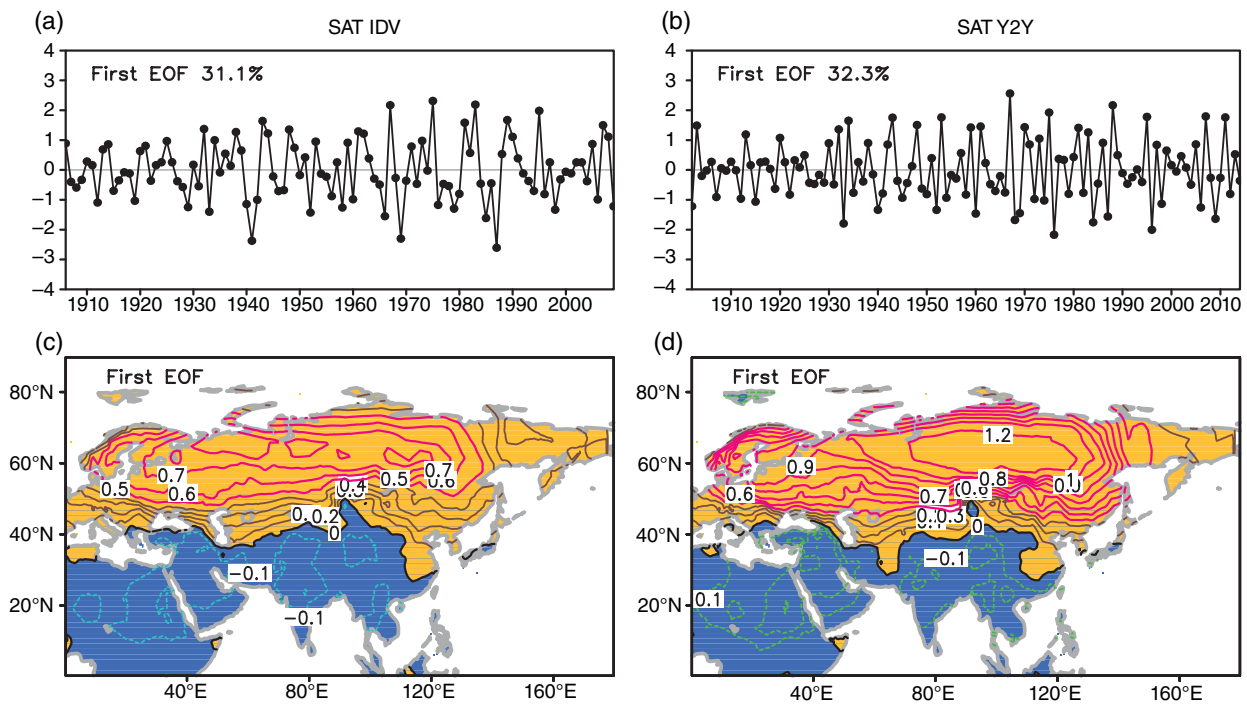


Figure 3. (a) Spatial distribution (bottom) and the associated time series (top) of the first EOF of SAT IDV. (b) Same as (a) except for SAT Y2Y. [Colour figure can be viewed at wileyonlinelibrary.com].

increasing trend for 1935–1975, while the standard deviation of the SAT Y2Y over CHN showed a moderate increasing trend.

3.2. Multi-decadal variation and secular trend

Figure 6(a) shows the multi-decadal variation modes derived from EEMD decompositions of the SAT over SIB, CHN and CA. The SIB SAT exhibited relatively intense multi-decadal variations (approximately 1.0 K) among the three areas, with the cycle of approximately 60 years. The CA SAT showed a 20-year cycle. The discrepancy in the multi-decadal variations may contribute to part of the out-of-phase relationship between the SIB SAT and CA SAT seen in Figure 1(b). Nevertheless, the multi-decadal variations of the CA SAT were much weaker than that of the SIB SAT (by approximately 0.4 K), indicating a limited contribution of multi-decadal variations to the warming over CA. The cycle of the SAT over CHN was approximately 80 years, longer than those over SIB and CA. Additionally, the multi-decadal variation magnitudes of the CHN SAT were approximately 0.8 K, which is twice of that of the CA SAT and only slightly smaller than that of the SIB SAT. These results suggested that the contribution of multi-decadal variations to the total SAT variation over CHN and SIB was probably much larger than that to the total SAT variations over CA. The secular trend in SIB and CHN generally showed linear warming trends, with 1.88 K for SIB and 0.64 K for CHN (Figure 6(b)). Unlike the SIB and CHN SAT, the secular trend in the CA SAT was parabolic, with the minimum in 1927–1928 and then continual warming (Figure 6(b)). Furthermore, the warming trend of the CA SAT after 1950

is as intensive as that of the SIB SAT, with the secular trend in 2014 being 1.12 K warmer than that in 1901 and 1.26 K warmer than that in 1927–1928. In comparison, the secular trend is much less over CHN than those over SIB and CA.

For the variations in the SIB SAT, the multi-decadal variation explained 11.3% of the variance and the secular trend explained 28.5% of the variance (Table 1), suggesting that the standard deviation of the multi-decadal variations were more than one-third of the secular trend in the SIB SAT. In other words, the intense multi-decadal variation had a considerable effect on the warming of the SIB SAT. Thus, the sum of the multi-decadal variation and secular trend in the SIB SAT showed two wave crests in the 1940s and the 1990s, two warming troughs in the 1960s and after 2005, and a hiatus for 1990–2005 because of the modulation of the multi-decadal variations (Figure 6(c)). However, more than 60% of the variance is explained by the IDV, indicating that the signals of the multi-decadal variations and secular trend were relatively damped in comparison with the intensive IDV (Table 1). Over CHN, the contributions of IDV, multi-decadal variations and secular trend to the CHN SAT variance were equivalent, with 35.1% for the IDV, 34.0% for the multi-decadal variation and 30.9% for the secular trend (Table 1); namely, the multi-decadal variation could explain more than 50% warming in CHN SAT, and both signals of the multi-decadal variations and secular trend were as significant as the signal of IDV, different from the results of SIB SAT. Because of the equivalent effect of multi-decadal variation and linear secular trend on the long-term variations in the CHN SAT, a total of the two wave crest appeared in the 1940s and 2000s, and

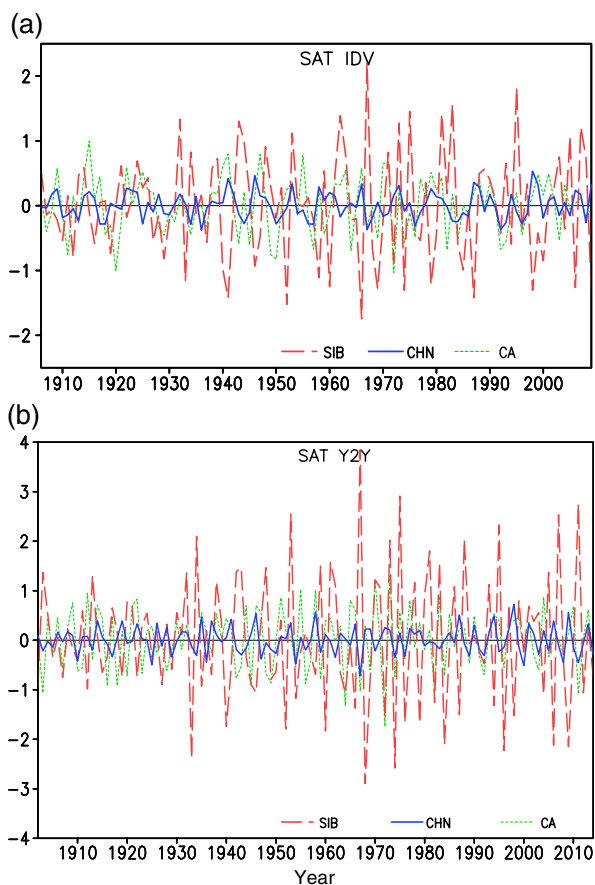


Figure 4. (a) Time series of the SAT IDV over SIB (long dash), CHN (solid) and CA (short dash). (b) Time series of the SAT Y2Y over SIB (long dash), CHN (solid) and CA (short dash). [Colour figure can be viewed at wileyonlinelibrary.com].

the two warming troughs appeared in the 1900s and the 1970s. After 2005, the CHN SAT exhibited a decreasing warming rate due to the combination of downwards positive phase of the multi-decadal variation and linear warming trend (Figure 6(c)). Over CA, the weak multi-decadal variations and intensive secular trend corresponded to the damped fluctuation and primary warming trend of the sum of multi-decadal variation and secular trend. The secular trend explained 45.6% of the variance, indicating its dominant role in the variation of the CA SAT (Table 1). Only 7.3% variance was explained by multi-decadal variation. The warming rate over CA may be the steadiest because of the damped modulations of multi-decadal variation on the warming.

4. Plausible causes for the variations at multi-time scales

Figure 7 shows the leading EOF modes of SAT over Eurasia and the northern part of Africa in the HIS, NAT, GHG and CTRL. In the HIS, the SAT exhibited homogeneous but uneven spatially multi-decadal variations and warming trend with gradually increasing anomalies from south to north (Figure 9(a)). Moreover, 38.3% of the variance was explained by this pattern, which is close

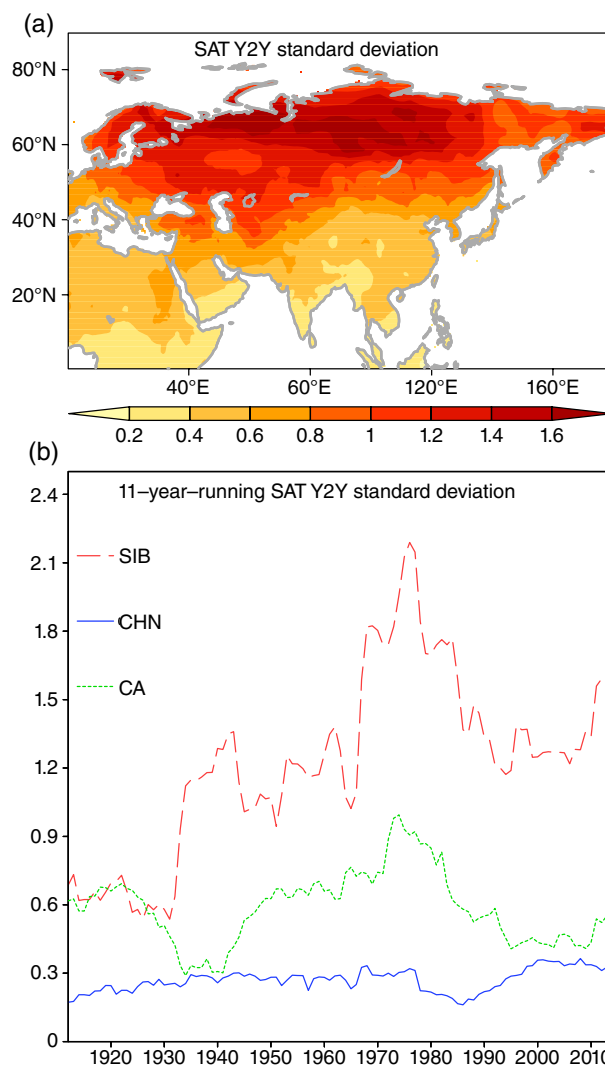


Figure 5. (a) Spatial distribution of the SAT Y2Y standard deviation. (b) Time series of the 11-year-running standard deviation of the SAT Y2Y over SIB (long dash), CHN (solid) and CA (short dash). [Colour figure can be viewed at wileyonlinelibrary.com].

to the 39% of the variations in the observation. Generally, the pattern was similar to that in the observation, except the intensity was slightly smaller in the HIS. The homogeneous multi-decadal variations in the NAT and the homogeneous warming trend in the GHG suggested that the multi-decadal variation was a response to the natural forcing while the warming trend was a response to the well-mixed increasing greenhouse gases (Figures 7(b) and (c)). Furthermore, the homogeneous multi-decadal variations in the NAT and the homogeneous warming trend in the GHG show a northwards increase, which were similar to those in the observations. Namely, the northwards increase of the multi-decadal variations and warming trend were also the consequences of natural and greenhouse gas forcing, respectively. Additionally, 67.8% of the variance was explained by the leading EOF mode in the GHG, indicating that the major warming was the response of the atmosphere to the increasing greenhouse gases. Comparing the leading EOFs in the three experiments, the positive

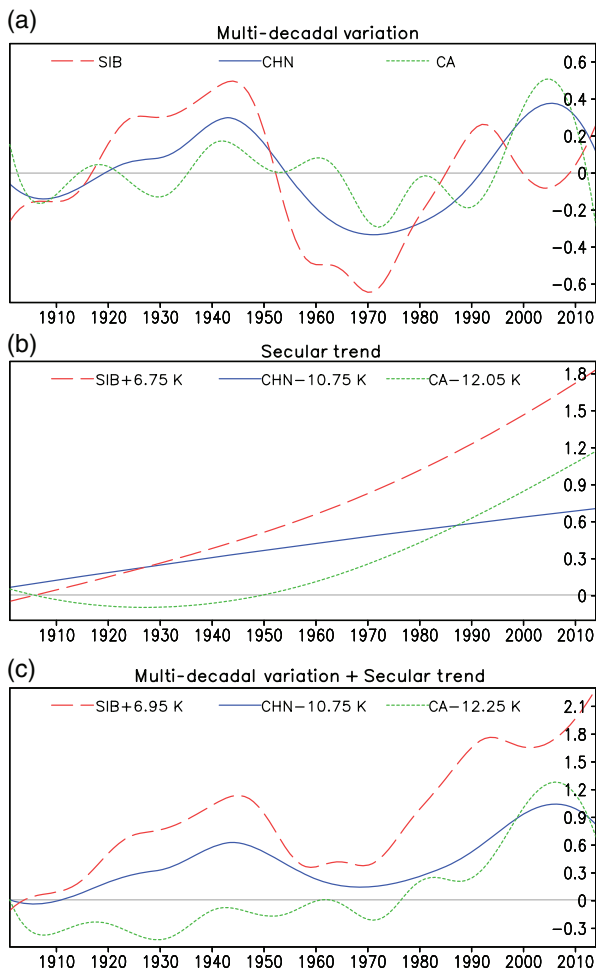


Figure 6. (a) Multi-decadal variations, (b) secular trends and (c) the sum of multi-decadal variations and secular trends derived from EEMDs of the SAT over SIB (long dash), CHN (solid) and CA (short dash). [Colour figure can be viewed at wileyonlinelibrary.com].

(negative) phase in the NAT corresponded to the positive (negative) phase in HIS before the 1970s, suggestive of the dominant effect of natural forcing in comparison with the greenhouse gas forcing. After the 1970s, corresponding to the accelerated concentration of greenhouse gases, the HIS exhibited positive anomalies while the NAT had negative phase, indicating the more important effect of greenhouse gases after the 1970s. The second EOF mode in the HIS showed a north–south dipole, with positive anomalies north of 45°N and negative anomalies south of 45°N and over the landmass north of the Okhotsk Sea. The pattern showed intensive IDV, multi-decadal variation and a moderate decreasing trend (Figure 7(a)). The patterns in both the second EOF modes of the NAT and GHG were similar to those in the HIS (Figures 7(b) and (c)). Specially, the negative anomalies north of the Okhotsk Sea and the moderate decreasing trend seemed to have been the consequences of increasing greenhouse gas forcing. The patterns in the second EOF modes of the HIS, NAT and GHG were similar to those in the observations, except for the much weaker negative centre around CA. Generally, the leading and second EOF modes in the CTRL exhibited

large differences from those of the observations, suggesting that the multi-decadal variations and warming trend were the consequences of forcings (Figure 7(d)).

Figures 8(a)–(c) show the leading EOF modes of the SAT Y2Y in the HIS, NAT and GHG, respectively. The SAT Y2Y in all three experiments exhibited north–south dipoles across $\sim 35^{\circ}\text{N}$, which were generally similar to those in the observation. It seems that both natural and greenhouse gas forcing could cause the dipole pattern. However, the SAT Y2Y in the CTRL also showed a north–south dipole (Figure 8(d)), which was similar to that in the observations. That is, the north–south dipole of the SAT Y2Y was the consequence of the internal interactions within the complex nonlinear climate system. The spatial distribution of the pattern in the GHG has more similarities with that in the CTRL, suggestive of weaker influence of greenhouse gas forcing on the spatial pattern of the SAT Y2Y in comparison with that in the NAT. In fact, more than 45% of the variance of the leading EOF in the NAT was explained by IMF1, indicating the considerable effect of the natural forcing on SAT Y2Y. The regions with negative anomalies in the NAT were much smaller than those in the CTRL. Consequently, the negative anomalies south of 40°N in the HIS were weaker than those observed. In other words, the impact of natural forcing on the SAT IDV might have been exaggerated in the GFDL numerical model outputs.

In comparison with the observation, the standard deviation of SAT Y2Y in the CTRL were much weaker, with the values of less than 0.2 K south of 40°N and less than 0.4 K in most parts of the regions north of 40°N (Figure 9(d)). Both the natural and greenhouse gas forcings could intensify the SAT Y2Y. However, both kinds of forcing exaggerated the variations south of 40°N whereas they underestimated the variations in Europe and western SIB (Figures 9(b) and (c)). Generally, the values of the standard deviations of the SAT Y2Y in the NAT and GHG were greater than 0.2–0.4 K south of 40°N and less than 0.2–0.4 K north of 40°N in comparison with the observation. The standard deviation in the HIS was similar to those in the NAT and GHG (Figure 9(a)). For the period 1910–2005, the 11-year-running standard deviation of the SAT Y2Y exhibited a peak in the 1980s over SIB and an increasing tendency before the 1980s over CA and a weakly increasing trend over CHN (Figure 9(e)), similar to the patterns in the observations. However, the variability of SAT Y2Y over CA after the 1980s and the robust fluctuation in CHN were quite different from those observed. Additionally, the large spread of the HIS, NAT and GHG in the three regions suggested the difficulty in estimating the relative importance of natural or greenhouse gas forcings in the time evolution of the SAT Y2Y.

Figure 10 illustrates the multi-decadal variations, secular trends and the sum of multi-decadal variations and secular trends of SIB, CHN and CA SAT in the HIS, NAT and GHG. The multi-decadal variations in the HIS over SIB and CHN were similar to those observed for 1901–2005. The simulated multi-decadal variations over the CA exhibited a time evolution similar to that over the CHN, which

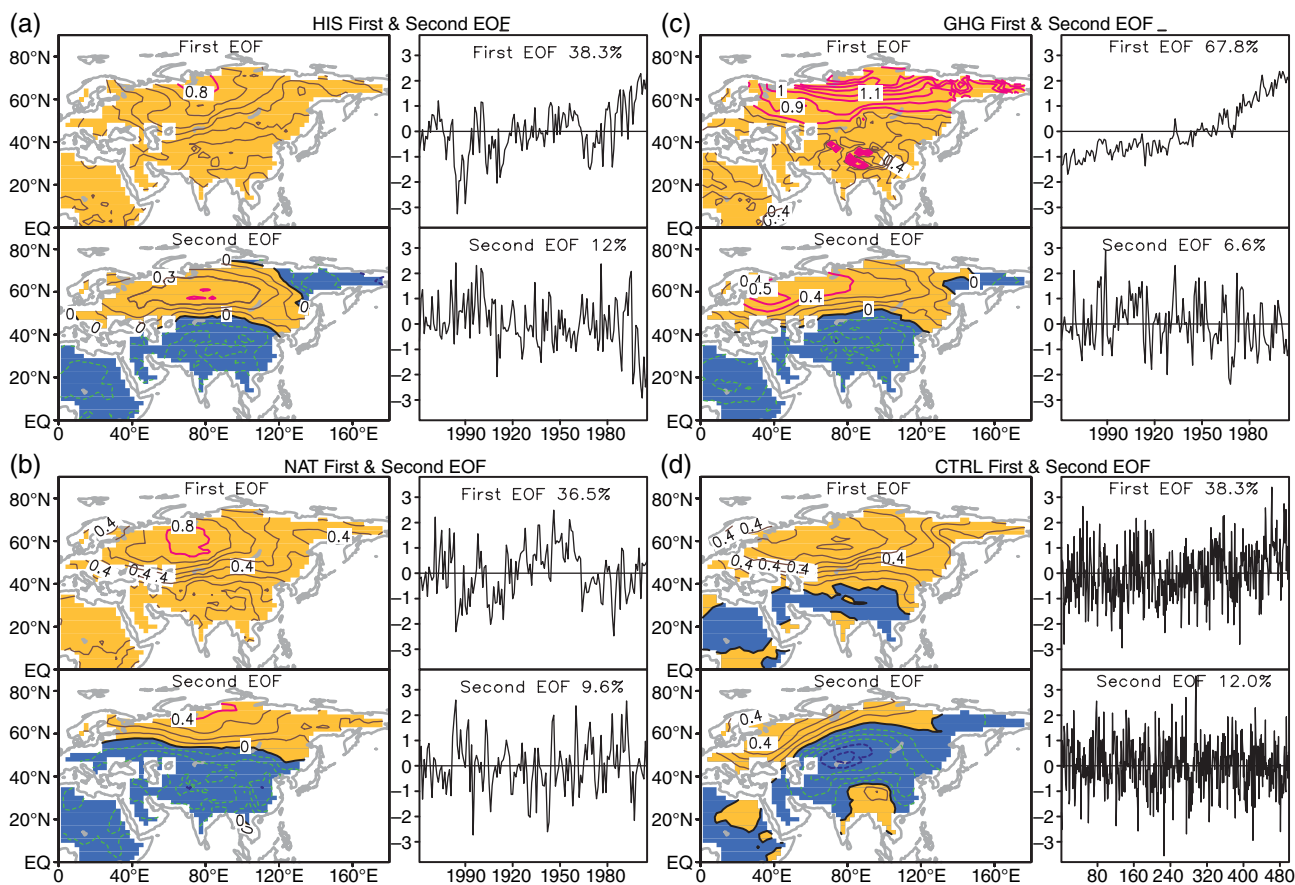


Figure 7. (a) Spatial distribution (left) and the time series (right) of the leading EOF (top) and the second EOF (bottom) modes of the SAT in the HIS. (b)–(d) Same as (a) except for the NAT, GHG and CTRL, respectively. [Colour figure can be viewed at wileyonlinelibrary.com].

was considerably different from the 20-year circle in the observation. The time series of the multi-decadal variations in the HIS showed considerable similarity to those in the NAT and little similarity to those in the GHG, suggestive of the dominant effect of natural forcing on the multi-decadal variations. The difference between the HIS and NAT occurred after the 1970s for SIB SAT. Although the SAT in both HIS and NAT exhibited upwards variations, the multi-decadal variations were in a positive phase in the HIS after 1980 whereas the variations were in a negative phase in the NAT. A similar situation also occurred in the 1900s. Namely, other forcings also contributed to the multi-decadal variations in the SIB SAT.

The secular trend intensities of the SIB, CHN and CA SAT in the HIS were much weaker than those observed. The secular trend of the CHN SAT in the HIS could be generally ignored for 1861–2005. For 1901–2005, aside from the secular trend of the CA SAT, the secular trend of the CHN SAT in the HIS also looked like a parabola, which was inconsistent with the linear trend of the CHN SAT in the observation. Note that the secular trend in the GHG exhibited a warming greater than 2.5 K for the SIB SAT and greater than 1.5 K for the CHN and CA SAT, which were much more greater than those in the HIS and the observations. That is, large parts of the warming caused by the greenhouse gas forcing were modulated by the cooling effects of some other forcing (e.g. anthropogenic aerosols)

and the cooling effect was exaggerated in the GFDL models considering the minor effect of natural forcing on the warming. Consequently, although the warming of the SIB SAT and CHN SAT in the HIS for 1901–2005 exhibited similar fluctuations to those observed, such as the two troughs in the 1910s and the 1960s, the two peaks in the 1940s and the 1990s, and the warming hiatus after the 1990s for the SIB SAT, as well as the wave crest in the 1970s and the continuous warming after 1980s for the CHN SAT, the warming trends were much weaker than those observed (Figure 10(a)). For the CA SAT, the sum of the multi-decadal variations and secular trend in the HIS showed a considerable discrepancy from the observations. Parts of the Tibetan and Iran Plateau, where the elevation is generally higher than 2000 m and the terrain is quite complex, were located in CA, which was an important reason for the inferior simulation skill in the CA SAT.

5. Summary and conclusion

Using the observed SAT data and four sets of simulated SAT from the GFDL coupled model, we investigated the variations of SAT over Eurasia and the northern part of Africa in multi-time scales and their plausible causes. The leading pattern of Eurasian SAT exhibited a homogeneous warming. However, the warming was modulated

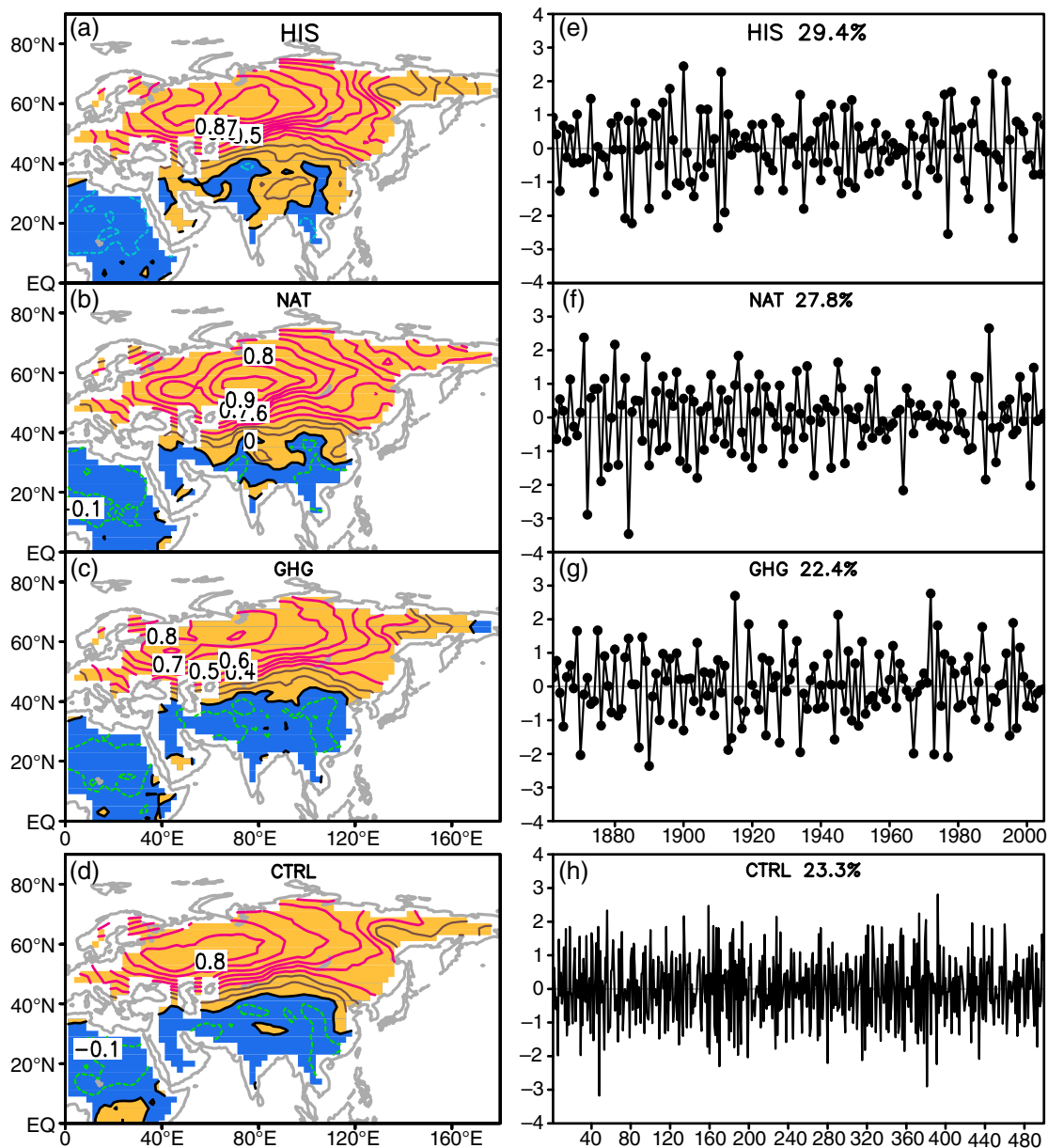


Figure 8. (a) Spatial distribution (left) and the associated time series (right) of the leading EOF mode in terms of the SAT Y2Y in the HIS. (b)–(d) Same as (a) except for the NAT, GHG and CTRL, respectively. [Colour figure can be viewed at wileyonlinelibrary.com].

by a robust multi-decadal variation and exhibited uneven spatial features. The observed patterns seemed to be a response to the joint impact of natural and greenhouse gas forcings on SAT as the leading pattern in the NAT exhibited homogenous multi-decadal variations, the leading pattern in the GHG showed a homogeneous warming and both the multi-decadal variation in the NAT and the warming in the GHG exhibited northwards increases with their largest intensities over SIB and the smallest intensities over CHN.

The evolution of the multi-decadal variations in the observed SIB SAT exhibited a general 60-year cycle, with positive phases during 1920–1950 and after 1980 and negative phases before 1920 and during 1950–1980. The multi-decadal variations in the CHN SAT showed positive phases during 1920–1950 and after 1990 and negative phases before 1920 and during 1950–1990.

Generally, natural forcing could explain the evolution of the multi-decadal variations over SIB and CHN, although the simulated multi-decadal variations were a marginally weaker than those observed. The contribution of greenhouse gases to the multi-decadal variations accounted for very little. In comparison, the intensities of the multi-decadal variations over SIB and CHN were much stronger than those over CA. A moderate 20-year cycle was found in the multi-decadal variations in the CA SAT. The GFDL's model showed poor simulation ability for the multi-decadal variations over CA due to the complex terrain of this region. The secular trends over SIB and CHN were linear, whereas the secular trend over CA was parabolic, with the minimum in 1927–1928. The greenhouse gases forcing dominated the secular trend.

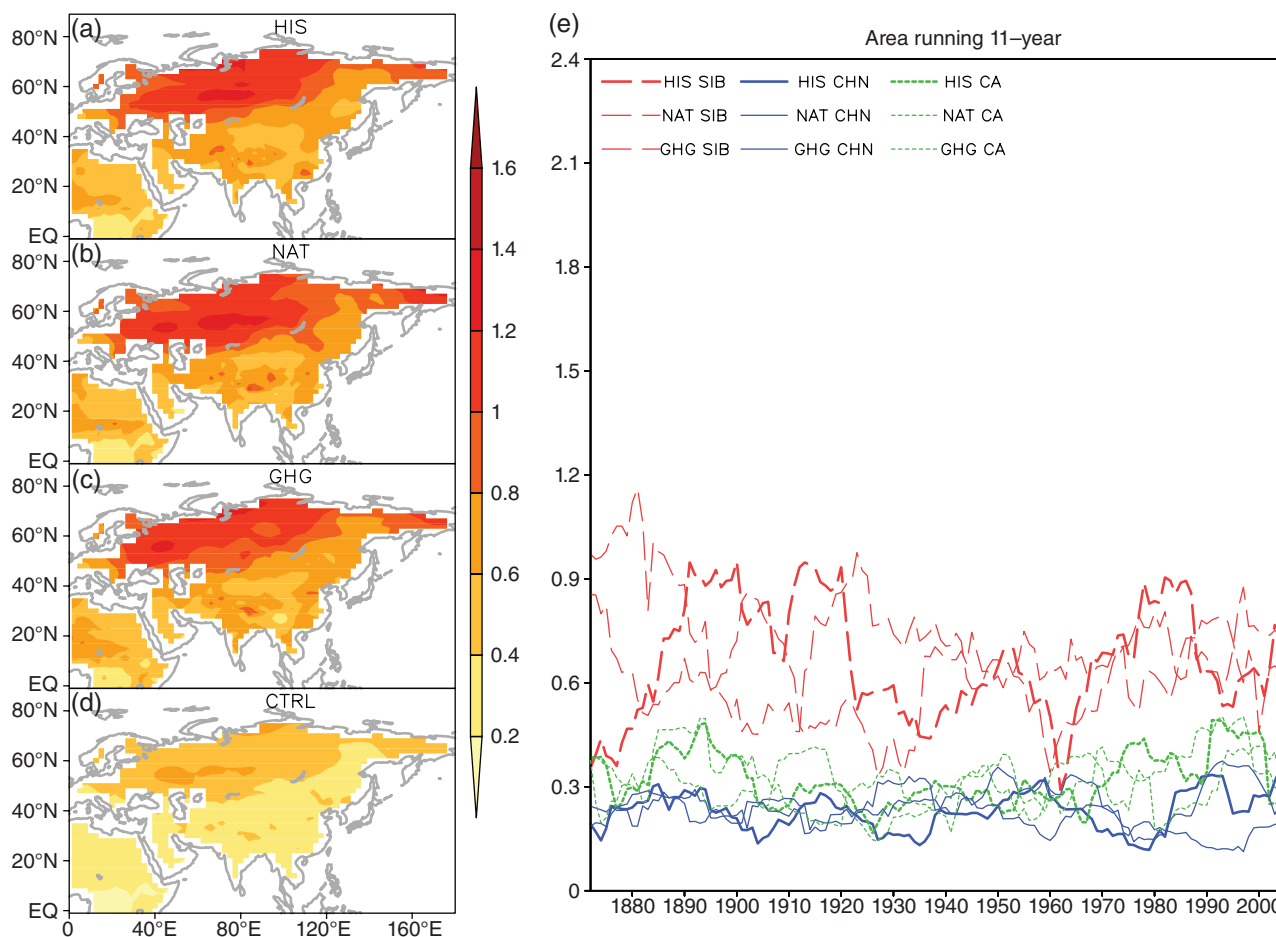


Figure 9. Spatial distribution of the SAT Y2Y standard deviations in the HIS (a), NAT (b), GHG (c) and CTRL (d), (e) the time series of 11-year-running standard deviation of SAT Y2Y over SIB (thick long dash), CHN (thick solid) and CA (thick short dash) in the HIS, NAT (same as in HIS but with medium lines) and GHG (same as in HIS but with thin lines). [Colour figure can be viewed at wileyonlinelibrary.com].

Overall, the half of the warming over CHN can be explained by the multi-decadal variations because the intensities of the multi-decadal variations and secular trend over CHN were generally equivalent. Over SIB, the hiatus for the period 1990–2005 may be the consequence of the downwards multi-decadal variations because more than one-fourth of the warming could be explained by the multi-decadal variations. The greenhouse gas forcing dominated the warming but the natural forcing played a considerable role in modulating the warming over SIB. The modulation of the multi-decadal variations on the warming over CA was small because of the damped multi-decadal variations.

The leading pattern of the SAT IDV exhibited a north–south dipole across 40°N, with an intense positive variation north of 40°N and a moderate negative variation south of 40°N. Specifically, the SAT Y2Y in SIB showed a significant negative relationship with that in CHN. The coupled model documented that the north–south dipole of the SAT Y2Y was the consequence of internal interactions within the complex nonlinear climate system. The natural forcing played a slightly modulatory role whereas the effect of greenhouse gases was relatively small. The observed standard deviation of the SAT Y2Y

exhibited a gradual increase from south to north, with the value in SIB five times of that in CHN. The northwards increase of the SAT Y2Y was also due to internal interactions within the complex nonlinear climate system, but both natural and greenhouse gas forcings intensified the variations. The variation south of 40°N was exaggerated whereas the variation north of 40°N was weakened in the model. In short, the meridional gradient of the SAT Y2Y in the HIS was much weaker than that observed. The evolutions of the SIB and CA SAT Y2Y standard deviations generally increased before 1975 and then decreased after. Over CHN, the standard deviation of the SAT Y2Y exhibited a moderate increasing trend. The evolution of the SAT Y2Y caused by the joint effects of all the forcings exhibited a reasonable similarity with those observed. However, neither the natural forcing alone nor the greenhouse gas forcing could lead to a reasonable simulation of the evolution of the SAT Y2Y on their own.

The intensive IDV and their significant discrepancies between different regions disclosed by this study may provide an important clue for the future studies of the high-impact extreme climate events over Europe and Asia because of the importance of Eurasian surface heating to

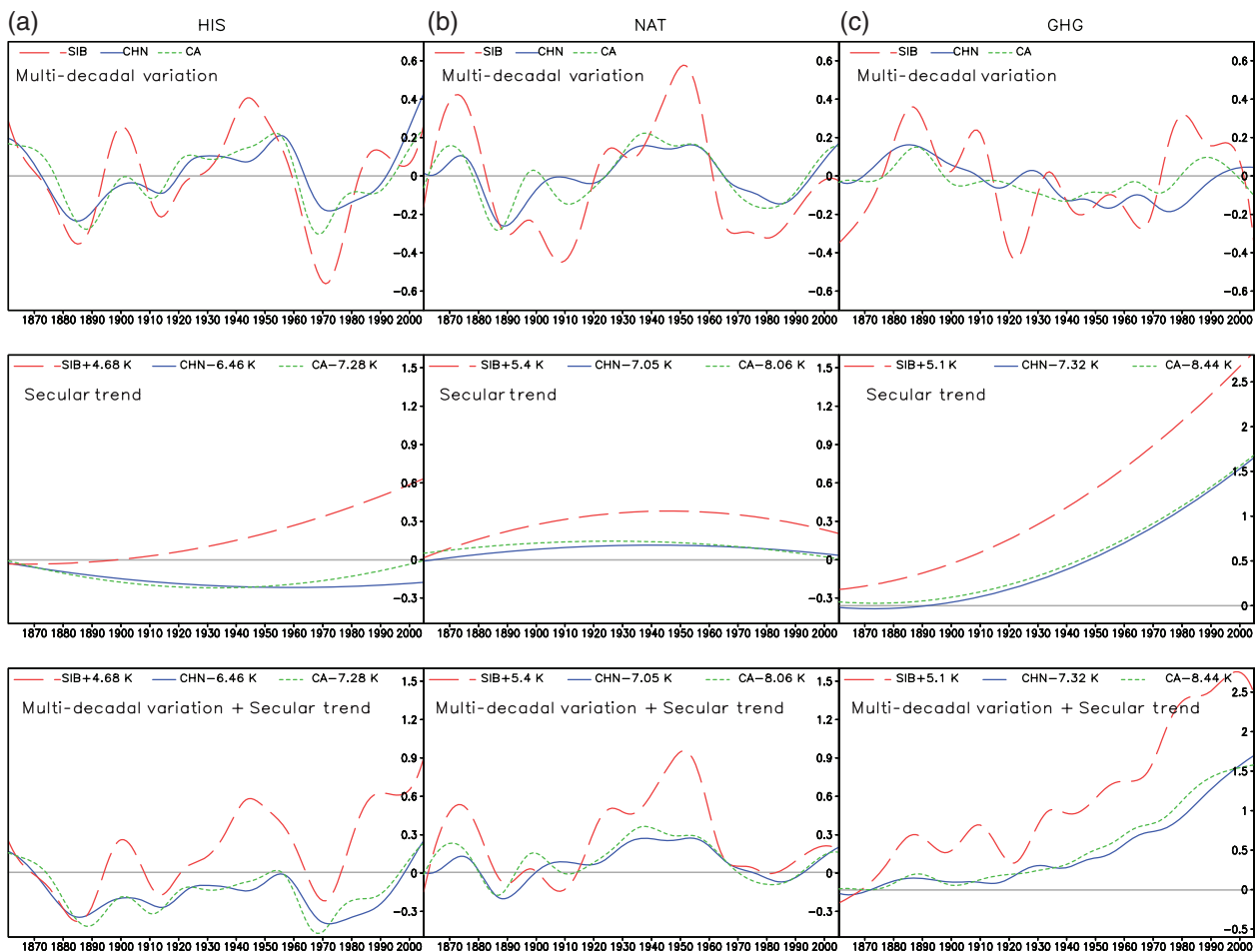


Figure 10. Multi-decadal variations (top), secular trends (middle) and the sum of the multi-decadal variations and secular trends (bottom) derived from the EEMDs of the SAT over SIB (long dash), CHN (solid) and CA (short dash) in the HIS (left), NAT (middle) and GHG (right). [Colour figure can be viewed at wileyonlinelibrary.com].

the weather. For the longer than decadal time scales, the different warming speeds between SIB SAT and CHN SAT could change the meridional gradient of SAT, which may considerably contribute to climate change over Asia. The effect of Eurasian SAT variations on these high-impact extreme events and on climate change deserve to further investigation in the future.

Acknowledgements

This study was jointly supported by the National Key Research and Development Program (2016YFA0601502), the National Natural Science Foundation of China (41375092, 41221064 and 41405078), and by the Basic Research Fund of Chinese Academy of Meteorological Sciences (2015Z001).

References

- Booth BBB, Dunstone NJ, Halloran PR, Andrews T, Bellouin N. 2012. Aerosols implicated as a prime driver of twentieth-century North Atlantic climate variability. *Nature* **484**: 228–232.
- Donner LJ, Wyman BL, Hemler RS, Horowitz LW, Ming Y, Zhao M, Golaz J-C, Ginoux P, Lin S-J, Schwarzkoepf MD, Austin J, Alaka G,

- Cooker W, Delworth TL, Freidenreich SM, Gordon CT, Griffies SM, Held IM, Hurlin WJ, Klein SA, Knutson TR, Langenhorst AR, Lee H-C, Lin Y, Magi BI, Malyshev SL, Milly PCD, Naik V, Nath MH, Pincus R, Plosha JJ, Ramaswamy V, Seman CJ, Shevliakova E, Sirutis JJ, Stern WF, Stouffer RJ, Wilson RJ, Winton M, Wittenberg AT, Zeng F. 2012. Dynamical core, physical parameterizations, and basic simulation characteristics of the atmospheric component AM3 of the GFDL global coupled model CM3. *J. Clim.* **24**: 3484–3519.
- Dunne JP, John JG, Adcroft AJ, Griffies SM, Hallberg RW, Shevliakova E, Stouffer RJ, Cooker W, Dunne KA, Harrison M, Krasting JP, Malyshev SL, Milly PCD, Philipps P, Sentman LT, Samuels BL, Spelman MJ, Winton M, Wittenberg AT, Zadeh N. 2012. GFDL's ESM2 global coupled climate-carbon earth system models. Part I: physical formulation and baseline simulation characteristics. *J. Clim.* **25**: 6646–6665.
- Dunne JP, John JG, Shevliakova E, Stouffer RJ, Krasting JP, Malyshev SL, Milly PCD, Sentman LT, Adcroft AJ, Cooke W, Dunne KA, Griffies SM, Hallberg RW, Harrison MJ, Levy H, Wittenberg AT, Phillips PJ, Zadeh N. 2013. GFDL's ESM2 global coupled climate-carbon earth system models. Part II: carbon system formulation and baseline simulation characteristics. *J. Clim.* **26**: 2247–2267.
- Gao LH, Yan ZW, Quan XW. 2015. Observed and SST-forced multi-decadal variability in global land surface air temperature. *Clim. Dyn.* **44**: 359–369. <https://doi.org/10.1007/s00382-014-2121-9>.
- Hansen J, Ruedy R, Sato M, Lo K. 2010. Global surface temperature change. *Rev. Geophys.* **48**: RG4004. <https://doi.org/10.1029/2010RG000345>.
- IPCC. 2007. In *Climate Change: The Physical Science Basis*, Solomon S, Qin D, Manning M, Marquis M, Chen Z. (eds). Cambridge University Press: Cambridge.

- IPCC. 2013. In *Climate Change: The Physical Science Basis*, Solomon S, Stocker T, Qin D, Plattner G, Tignor M, Allen S, Boschung J, Nauels A, Xia Y, Bex V, Midgley P. (eds). Cambridge University Press: Cambridge.
- Ji F, ZH W, Huang JP, Chassignet EP. 2014. Evolution of land surface air temperature trend. *Nat. Clim. Change* **4**: 462–466. <https://doi.org/10.1038/NCLIMATE2223>.
- Jones PD, Lister DH, Osborn TJ, Harpham C, Salmon M, Morice CP. 2012. Hemispheric and large-scale land-surface air temperature variations: an extensive revision and an update to 2010. *J. Geophys. Res.* **117**: D05127. <https://doi.org/10.1029/2011JD017139>.
- Kang I-S. 1996. Association of interannual and interdecadal variations of global-mean temperature with tropical Pacific SST appearing in a model and observations. *J. Clim.* **9**: 455–464.
- Kravtsov S, Spannagle C. 2008. Multidecadal climate variability in observed and modeled surface temperatures. *J. Clim.* **21**: 1104–1121. <https://doi.org/10.1175/2007JCLI1874.1>.
- Levitus S, Antonov JI, Boyer TP, Stephens C. 2000. Warming of the world ocean. *Science* **287**: 2225–2229.
- Meehl GA, Arblaster JM, Fasulla JT, AX H, Trenberth KE. 2011. Model-based evidence of deep-ocean heat uptake during surface-temperature hiatus periods. *Nat. Clim. Change* **1**: 360–364. <https://doi.org/10.1038/nclimate1229>.
- Pepin N, Bradley RS, Diaz HF, Baraer M, Caceres EB, Forsythe N, Fowler H, Greenwood G, Hashmi MZ, Liu XD, Miller JR, Ning L, Ohmura A, Palazzi E, Rangwala I, Schöner W, Severskiy I, Shahgedanova M, Wang MB, Williamson SN, Yang DQ. 2015. Elevation-dependent warming in mountain regions of the world. *Nat. Clim. Change* **5**: 424–430. <https://doi.org/10.1038/nclimate2563>.
- Qian WH, Lu B, Zhu CW. 2010. How would global-mean temperature change in the 21st century? *Chin. Sci. Bull.* **55**: 1963–1967.
- Räisänen J. 2002. CO₂-induced changes in interannual temperature and precipitation variability in 19 CMIP2 experiments. *J. Clim.* **15**: 2395–2411.
- Shen X-S, Kimoto M. 2007. Studies of the interannual variability of spring Eurasian surface air temperature. *Chin. J. Atmos. Sci.* **31**: 19–27 (in Chinese).
- Smith TM, Reynolds RW, Peterson TC, Lawrimore J. 2008. Improvements to NOAA's historical merged land-ocean surface temperature analysis (1880–2006). *J. Clim.* **21**(10): 2283–2296.
- Toggweiler JR, Russell J. 2008. Ocean circulation in a warming climate. *Nature* **451**: 286–288. <https://doi.org/10.1038/nature06590>.
- Vecchi GA, Soden BJ, Wittenberg AT, Held IM, Leetmaa A, Harrison MJ. 2006. Weakening of tropical Pacific atmospheric circulation due to anthropogenic forcing. *Nature* **441**: 73, 76. <https://doi.org/10.1038/nature04744>.
- Wentz FJ, Ricciardulli L, Hibern K, Mears C. 2007. How much more rain will global warming bring? *Science* **317**: 233–235.
- Wu ZH, Huang NE, Wallace JM, Smoliak BV, Chen XY. 2011. On the time-varying trend in global-mean surface temperature. *Clim. Dyn.* **37**: 759–773. <https://doi.org/10.1007/s00382-011-1128-8>.
- Xiao D, Zhou XJ, Zhao P. 2012. Numerical simulation study of temperature change over East China in the past millennium. *Sci. China Earth Sci.* **55**: 1504–1517. <https://doi.org/10.1007/s11430-012-4422-3>.
- Zuo ZY, Zhang RH, Zhao P. 2011. The relation of vegetation over the Tibetan Plateau to the rainfall in China in boreal summer. *Clim. Dyn.* **36**: 1207–1219.
- Zuo ZY, Zhang RH, BY W, Rong XY. 2012a. Decadal variability in springtime snow over Eurasia: relation with circulation and possible influence on springtime rainfall over China. *Int. J. Climatol.* **32**: 1336–1345. <https://doi.org/10.1002/joc.2355>.
- Zuo ZY, Yang S, Kumar A, Zhang RH, Xue Y, Jha B. 2012b. Role of thermal condition over Asia in the weakening Asian summer monsoon under global warming background. *J. Clim.* **25**: 3431–3436.
- Zuo ZY, Yang S, Zhang RH, Jiang PP, Zhang L, Wang F. 2013. Long-term variations of broad-scale Asian summer monsoon circulation and possible causes. *J. Clim.* **26**: 8947–8961. <https://doi.org/10.1075/JCLI-D-12-00691.1s>.